


The ALPINE-ALMA [CII] survey: Double stellar population and active galactic nucleus activity in a galaxy at $z \sim 5.5$

L. Barchiesi^{1,2} , M. Dessauges-Zavadsky³, C. Vignali^{1,2}, F. Pozzi^{1,2}, R. Marques-Chaves³, A. Feltre^{4,2}, A. Faisst⁵, M. Béthermin⁶, P. Cassata^{7,8}, S. Charlot⁹, Y. Fudamoto^{10,11}, M. Ginolfi¹², E. Ibar¹³, G. C. Jones¹⁴, M. Romano¹⁵, D. Schaerer³, L. Vallini¹⁶, E. Vanzella², and L. Yan¹⁷

¹ Dipartimento di Fisica e Astronomia, Università degli Studi di Bologna, Via P. Gobetti 93/2, 40129 Bologna, Italy
e-mail: luigi.barchiesi2@unibo.it

² INAF-OAS, Osservatorio di Astrofisica e Scienza dello Spazio di Bologna, Via Gobetti 93/3, 40129 Bologna, Italy

³ Department of Astronomy, University of Geneva, Chemin Pegasi 51, 1290 Versoix, Switzerland

⁴ SISSA, Via Bonomea 265, 34136 Trieste, Italy

⁵ IPAC, California Institute of Technology 1200 E California Boulevard, Pasadena, CA 91125, USA

⁶ Aix-Marseille Univ., CNRS, LAM, Marseille, France

⁷ Dipartimento di Fisica e Astronomia, Università di Padova, Vicolo dell'Osservatorio 3, 35122 Padova, Italy

⁸ INAF – Osservatorio Astronomico di Padova, Vicolo dell'Osservatorio 5, 35122 Padova, Italy

⁹ Institut d'Astrophysique de Paris, Sorbonne Université, CNRS, UMR7095, 75014 Paris, France

¹⁰ Waseda Research Institute for Science and Engineering, Faculty of Science and Engineering, Waseda University, 3-4-1 Okubo, Shinjuku, Tokyo 169-8555, Japan

¹¹ National Astronomical Observatory of Japan, 2-21-1, Osawa, Mitaka, Tokyo, Japan

¹² European Southern Observatory, Karl-Schwarzschild-Strasse 2, 85748 Garching, Germany

¹³ Instituto de Física y Astronomía, Universidad de Valparaíso, Avda. Gran Bretaña 1111, Valparaíso, Chile

¹⁴ Department of Physics, University of Oxford, Denys Wilkinson Building, Keble Road, Oxford OX1 3RH, UK

¹⁵ National Centre for Nuclear Research, ul. Pasteura 7, 02-093 Warsaw, Poland

¹⁶ Scuola Normale Superiore, Piazza dei Cavalieri 7, 56126 Pisa, Italy

¹⁷ The Caltech Optical Observatories, California Institute of Technology, Pasadena, CA 91125, USA

Received 30 August 2022 / Accepted 29 November 2022

ABSTRACT

Context. GDS J033218.92-275302.7 (here GS-14) is a $z \sim 5.5$ galaxy with unusual UV spectral features that have been interpreted as signatures of either a double stellar population or of an active galactic nucleus (AGN). GS-14 was detected in [C II] $158 \mu\text{m}$ as part of the ALPINE survey and was found to be the galaxy with the lowest molecular gas fraction ($f_{\text{mol}} = M_{\text{molgas}} / (M_{\text{molgas}} + M_*) \sim 0.1$) of that sample.

Aims. We exploited the multiwavelength coverage of GS-14 to investigate the properties and the origin of its emission.

Methods. We fit the UV-to-near-IR spectral energy distribution (SED) with a single and double stellar population and/or AGN component. We analyzed the latest release of the VIMOS spectrum, which shows highly ionized emission lines (O VI 1032 Å, N V 1240 Å, and N IV] 1483, 1486 Å). The line equivalent widths and line ratios were compared with those observed in galaxies and AGN, as well as with the predictions from radiation transfer models for star-forming galaxies, AGN, and shocks.

Results. The SED-fitting provides a total stellar mass of $M_* = (4 \pm 1) \times 10^{10} M_\odot$, an age of the main stellar population of ~ 670 Myr, and a recent (~ 8 Myr) short burst of star formation (SF) of $\sim 90 M_\odot \text{yr}^{-1}$. We do not find a significant contribution from an AGN, although we do not have any coverage in the mid-IR, where the dust emission of the AGN would peak. The N V line has a characteristic P Cygni profile. Fitting it with stellar models suggests a ~ 3 Myr old population of stars with a mass of $\sim 5 \times 10^7 M_\odot$, consistent with a second component of young stars, as found in the SED-fitting analysis. The N V profile also shows evidence for an additional component of nebular emission. The comparison of the line ratios (N IV]/N V and O VI/N V) with theoretical models allows us to associate the emission with SF or AGN, but the strong radiation field required to ionize the O VI is more commonly related to AGN activity.

Conclusions. Studying GS-14, we found evidence for an old and already evolved stellar population at $z \sim 5.5$, and we show that the galaxy is experiencing a second short burst of SF. In addition, GS-14 carries signatures of obscured AGN activity. The AGN could be responsible for the short depletion time of this galaxy, thus making GS-14 one of the two ALPINE sources with indications of an active nucleus and an interesting target for future follow-ups to understand the connection between SF and AGN activity.

Key words. galaxies: high-redshift – galaxies: active – galaxies: evolution

1. Introduction

It is established that the growth of supermassive black holes (SMBH) and the evolution and properties of their host galaxies must be coupled, but the exact mechanism, timescales, and how

they influence each other are still debated. Scaling relations between the mass of the SMBH and several physical properties of the host galaxy, such as galaxy bulge mass, luminosity, and velocity dispersion (e.g., Kormendy & Richstone 1995; Magorrian et al. 1998; Ferrarese & Merritt 2000; Gebhardt et al. 2000;

Kormendy & Ho 2013), led to the formulation of the active galactic nucleus (AGN)-galaxy coevolution paradigm (e.g., Hopkins et al. 2007). In this coevolution scenario, on the one hand, the stellar feedback may help to funnel gas toward the nuclear region of the galaxy, thus triggering the AGN activity. On the other hand, the AGN feedback heats up and expels the gas (Zana et al. 2022), which reduces or quenches the star formation (SF). Signatures of this interaction have been observed in winds and outflows of cold molecular gas (e.g., Feruglio et al. 2010; Ciccone et al. 2014) and neutral atomic (Rupke et al. 2005) and ionized (Weymann et al. 1991; McKernan et al. 2007) gas. The interplay between AGN and SF of main-sequence (MS) galaxies has been studied in the local Universe and at cosmic noon ($z \sim 2$), but scarcely at high redshift ($z \sim 5-6$), where most of our knowledge comes from luminous quasars (QSO) and starburst (SB) galaxies (e.g., Bischetti et al. 2022). A key step of the coevolution scenario is represented by the obscured-accretion phase, where most of the stellar mass formation and of the black hole (BH) accretion should take place. The main difficulty in studying this phase is that the AGN activity is shrouded by gas and dust and is likely embedded in the galaxy emission. It is therefore difficult to identify. This is particularly true for low-luminosity AGN (LLAGN): their mid-IR emission is diluted and overshadowed by the host-galaxy luminosity (i.e., Gruppioni et al. 2013). In addition, even the most recent X-ray facilities struggle to detect high- z LLAGN because their X-ray photon fluxes are low (Barchiesi et al. 2021).

High-redshift galaxies with ongoing SF and an indication of a possible AGN are the sources on which we focus when we search for hidden BH growth and for the impact of AGN on the SF (hence early galaxy evolution) itself. GDS J033218.92-275302.7 (hereafter GS-14) falls exactly within these parameters.

GS-14 is a $z = 5.56$ (Raiter et al. 2010; Vanzella et al. 2010) MS galaxy with unusual spectral features that have been interpreted as signatures of a double stellar population or linked to AGN activity. The nature of GS-14 emission has been extensively debated since its discovery in the southern field of the Great Observatories Origins Deep Survey (GOODS) during the ESO/FORS2 survey (Vanzella et al. 2006). Fontanot et al. (2007) selected this source as a QSO candidate on the basis of its z_{850} magnitude and color selection, but reclassified it as an H II star-forming galaxy due to the presence of the NIV] 1483, 1486 Å and the lack of the NV 1240 Å lines in the FORS2 spectrum (Vanzella et al. 2006). GS-14 appears as a compact-source at all wavelengths (Fig. 1), although it is marginally resolved both in the i_{775} and z_{850} bands (Vanzella et al. 2010). Wiklind et al. (2008) classified the source as a Balmer galaxy, with the discontinuity between the K_s and 3.6 μm filter indicating an evolved stellar population. Vanzella et al. (2010) interpreted the bright Ly α line and the detection of NIV] emission line as signature of a young population of massive stars or, alternatively, of an AGN. They also performed spectral energy distribution (SED) fitting using 16 photometric bands from UV to near-IR (NIR), and found that the source may host a double stellar population, composed of an evolved/aged population and of a young population of massive stars. Grazian et al. (2020) analyzed the same FORS2 spectrum as Vanzella et al. (2010) in depth together with new VIMOS and X-shooter spectra of this source. In addition to the two lines detected by Vanzella et al. (2010), they also found O VI 1032 Å, and N V 1240 Å emission lines, which led them to regard GS-14 as an AGN. Regarding the X-ray bands, GS-14 is undetected in the ultradeep 7 Ms X-ray image by *Chandra* with a flux limit of 10^{-17} erg cm $^{-2}$ s $^{-1}$ in the observer frame 0.5–2.0 keV band (Giallongo et al. 2019).

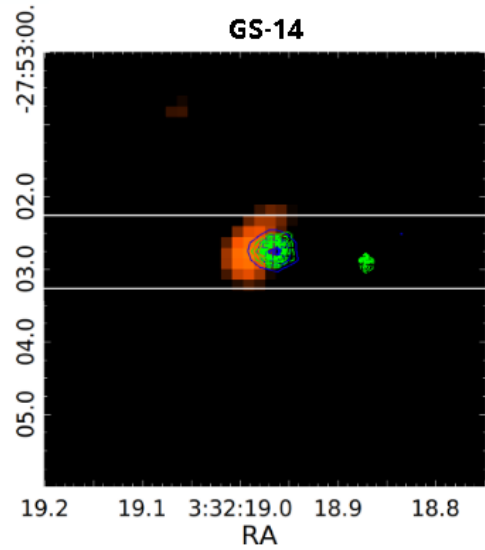


Fig. 1. GS-14 [C II] 158 μm flux map. The green contours represent the emission in the $r+$ SUBARU filter in which the Ly α line falls, and the blue contours show the emission in the ULTRAVISTA K_s filter (Cassata et al. 2020). The source is not resolved in any of the three wavelength ranges. Vanzella et al. (2010) associated an effective radius to the K_s emission of $r_e[3300 \text{ \AA}] < 0.9$ kpc.

GS-14 has also been selected as part of the ALMA Large Program to INvestigate C+ at Early Times survey (ALPINE; Le Fèvre et al. 2020; Faisst et al. 2020; Béthermin et al. 2020) as a normal star-forming galaxy (SFG). It has been detected in the [C II] 158 μm emission line with a signal-to-noise ratio (S/N) of 4.6, but it is not spatially resolved (with a beam of $0.7''$, ~ 4.2 kpc, Fig. 1). There is no detection of continuum near [C II] with an upper limit of $L_{\text{IR}} < 2.0 \times 10^{10} L_{\odot}$ in the far-infrared dust emission (Béthermin et al. 2020). With a molecular gas fraction of $f_{\text{mol}} = M_{\text{mol}}/(M_{*} + M_{\text{mol}}) = 0.10^{+0.13}_{-0.06}$ (derived from the [C II] luminosity; Dessauges-Zavadsky et al. 2020), GS-14 is the [C II]-detected source with the lowest f_{mol} of the entire ALPINE sample.

In this work we exploit the multiwavelength spectrophotometric coverage of GS-14 to investigate the physical origin of its emission. In Sect. 2 we report the spectral analysis of GS-14, and compare the observed lines with sources from the literature and with model predictions. The photometric analysis and SED fitting is reported in Sect. 3. We discuss our results and draw the conclusions in Sect. 4. Throughout this paper, we adopt a Chabrier (2003) initial stellar mass function and the following cosmological parameters: $H_0 = 70$ km s $^{-1}$ Mpc $^{-1}$, $\Omega_M = 0.3$, and $\Omega_{\Lambda} = 0.7$ (Spergel et al. 2003).

2. Spectral analysis

2.1. Spectroscopic data

Different rest-UV spectroscopic observations are available for GS-14 in terms of depth and resolution: a 4-hour FORS2 spectrum (Vanzella et al. 2010), a 20-hour VIMOS spectrum (ID 194.A-2003; McLure et al. 2018), and a 49-hour X-SHOOTER spectrum obtained under two observing programs (384.A-0886 and 089.A-0679). We focus on the VIMOS spectrum, as it has the best S/N of the three available spectra, and it allows us for the first time to detect the rest-frame UV continuum of this galaxy at $z \sim 5.5$ at a $S/N = 3.7$ (as computed in the 8200–9200 Å observed-frame wavelength range).

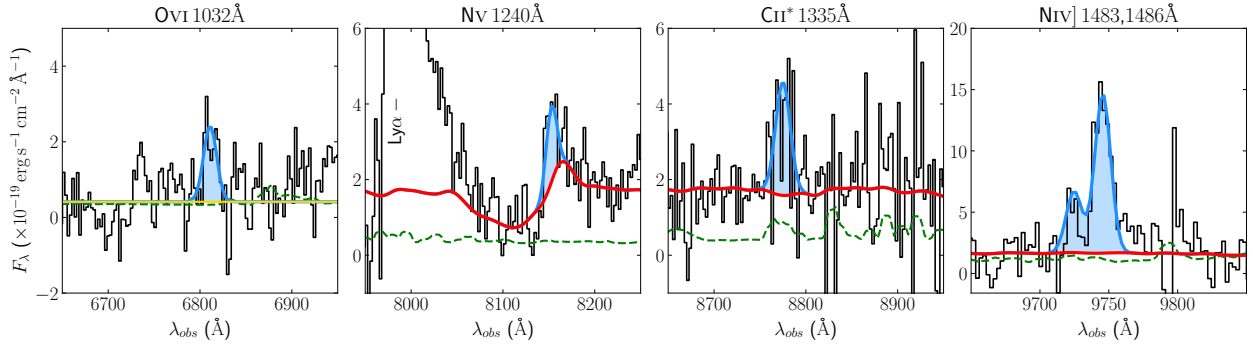


Fig. 2. Spectra and best-fit models for the GS-14 main spectral features analyzed in this work. From left to right: O VI 1032 Å, N V 1240 Å, C II* 1335 Å, and N IV] 1483, 1486 Å. The red line is the SS99 best-fit model, the Gaussian best fit for the emission feature is plotted in blue, the yellow line represents the continuum in the Lyman forest region, and the green line shows the spectrum noise. In the second panel, the strong emission line at $\lambda_{\text{obs}} \sim 8000$ Å is the Ly α line. For the complete VIMOS spectrum, see Fig. 2 in [Grazian et al. \(2020\)](#).

Figure 2 shows four windows of the one-dimensional spectrum of GS-14. The main features of the spectrum are the Ly α line and the almost total intergalactic medium (IGM) absorption blueward of it, at a wavelength of $\lambda_{\text{obs}} < 8000$ Å. N V 1240 Å and N IV] 1483, 1486 Å are detected at an S/N of 4.6 and 10.1, respectively ($S/N = F_{\text{line}} / (\int_{\lambda_0-3\sigma}^{\lambda_0-1.5\sigma} N_{\lambda} d\lambda + \int_{\lambda_0+1.5\sigma}^{\lambda_0+3\sigma} N_{\lambda} d\lambda)$, where F_{line} is the line-integrated flux, N_{λ} is the spectrum noise, λ_0 and σ are the line centroid and width). O VI 1032 Å and C II* 1335 Å are detected at an S/N of 4.4 and 4.0, respectively. C IV 1550 Å is not detected because this line falls at the edge of the VIMOS spectral range and over a sky emission line.

2.2. Spectral fitting

The latest release of the VIMOS spectrum reaches a continuum S/N of 3.7, which is high enough to show a clear P Cygni N V line profile for the first time. P Cygni profiles in N V are not unheard of ([Jaskot et al. 2017](#); [Vanzella et al. 2018](#); [Matthee et al. 2022](#)) and can be produced by stellar winds of very young and massive stars (e.g., [Prinja & Howarth 1986](#)) or be mimicked by broad or narrow absorption line quasar (BAL/NAL QSO; [Bentz et al. 2004](#); [Appenzeller et al. 2005](#)). As our spectrum does not show any absorption line and because there are no signs that GS-14 is a type 1 QSO (e.g., >1000 km s $^{-1}$ broad emission lines or high X-ray luminosity), the origins of the P Cygni profile are likely associated with a young population of massive stars. We fit the spectrum with the models from the STARBURST99 (S99) spectral synthesis code ([Leitherer et al. 1999](#)), adopting the same method as [Marques-Chaves et al. \(2021\)](#). S99 models allow the fitting of the stellar continuum and of the lines produced in the stellar atmosphere, but not lines that are produced in the ionized gas in the interstellar medium (ISM) of the galaxy. High-resolution UV model spectra with burst ages in the 0.01–20 Myr range and metallicities between 0.03 and $0.5 Z_{\odot}$ were rebinned and smoothed to the VIMOS spectrum resolution. To take dust attenuation into account, the [Calzetti et al. \(2000\)](#) extinction curve was used to match the $E(B - V)$ of the models with the one measured on the spectrum of GS-14 ($E(B - V) = 0.05$, from the 9200–12 000 Å observed-frame wavelength range). The free-from-lines spectral window 8400–8600 Å was used to normalize the flux of the S99 models to the GS-14 flux. Finally, we performed a χ^2 minimization on the 8050–8400 Å range to find the best fit for the N V line profile. We found that the VIMOS spectrum of GS-14 is

best fit with a 2.7 ± 0.1 Myr old stellar population, a mass of $(5 \pm 1) \times 10^7 M_{\odot}$, and a metallicity of $0.5 Z_{\odot}$. We note that the P Cygni fit exhibits a slight degeneracy with metallicity: the N V P Cygni profile varies little with different values of metallicity, while it is extremely sensitive to the age of the stellar population (see [Marques-Chaves et al. 2021](#)). Our best-fit model is able to reproduce the absorption part of the N V line profile as well as the continuum redward of the Ly α emission line. However, the best-fit S99 model is not able to fully reproduce the observed emission in N V, and we need an additional emission component. The Gaussian fit of this component provides an emission line centered at $8152.6_{-0.1}^{+0.6}$ Å, with a full width half maximum of $\text{FWHM} = 13.9_{-1.9}^{+2.4}$ Å and a flux of $2.9_{-0.1}^{+0.9} \times 10^{-18}$ erg cm $^{-2}$ s $^{-1}$.

We also fit the O VI, C II*, and N IV] emission lines using Gaussian components. Their best-fit values are reported in Table 1. Due to the IGM absorption, the measured O VI flux should be considered as a lower limit.

We compared the EW of the N V line in absorption and emission with the binary population and spectral synthesis code (BPASS; [Stanway & Eldridge 2018](#)) and with the S99 models. We find that some models are able to reproduce the observed EW in absorption and have a very young stellar population, in agreement with what we find from the P Cygni N V line profile. However, regarding the emission component, all the models have $\text{EW} > -3$ Å, which is far from the measured $\text{EW}_{\text{N V,em}} = -5.2$ Å. This result tells us that two different mechanisms are likely at the origin of the N V emission: Stellar winds from young and massive stars create the absorption component and contribute to the emission, while an additional emission that is not linked to stellar wind phenomena provides the rest of the observed N V flux. This additional contribution is likely due to the ionized gas in the ISM, which is not modeled by stellar synthesis codes such as BPASS or S99.

2.3. Comparison with the literature

We performed a deep search for sources in the literature with O VI 1032 Å, N V 1240 Å, or N IV] 1483, 1486 Å emission lines; our goal was to discern the nature (SF or AGN) of GS-14. We found eight sources with all the three lines, seven from [Dietrich et al. \(2003\)](#) at redshift $3.9 < z < 5$, and one from [Baldwin et al. \(2003\)](#) at $z = 1.96$. These are all spectroscopically confirmed AGN. The three lines can also be found in the [Hainline et al. \(2011\)](#) composite spectrum of 33 narrow-line AGN at $z \sim 2-3$. In the collection of sources, we also verified

Table 1. Properties of the emission lines of GS-14, derived from the VIMOS spectrum and fitting the lines with a Gaussian profile.

Line	λ_0 (Å)	FWHM (Å)	F (erg s ⁻¹ cm ⁻²)
O VI 1032 Å	6811.0 ^{+0.1} _{-1.0}	17.3 ^{+4.1} _{-2.2}	>3.6 ^{+0.9} _{-1.2} × 10 ⁻¹⁸
N V 1240 Å	8152.6 ^{+0.6} _{-0.1}	13.9 ^{+2.4} _{-1.9}	2.9 ^{+0.9} _{-0.1} × 10 ⁻¹⁸
C II* 1335 Å	8775.0 ^{+1.0} _{-1.0}	19 ⁺¹⁴ ₋₅	6.0 ^{+4.5} _{-3.0} × 10 ⁻¹⁸
N IV] 1483 Å	9724.8 ^{+0.4} _{-0.1}	13.9 ^{+2.4} _{-1.9}	7.3 ± 1.3 × 10 ⁻¹⁸
N IV] 1486 Å	9745.6 ^{+0.4} _{-0.1}	13.9 ^{+2.4} _{-1.9}	1.9 ± 0.3 × 10 ⁻¹⁷

Notes. λ_0 refers to the observed-frame centroid, FWHM is the full width at half maximum, and F is the line flux. For the NV emission line, the values refer to the fit obtained after the stellar component of the P Cygni profile was subtracted. The OVI line lies in the Lyman forest and its continuum is not detected. Its flux should therefore be considered a lower limit.

whether the flux of NIV] was higher than that of NV, as is the case for GS-14. None of the above-mentioned AGN shows this characteristic. We note that the $z = 3.36$ lensed galaxy of Fosbury et al. (2003) and the stacked spectrum of $z \sim 2-3.8$, $EW_{\text{CIII]} \geq 20 \text{ \AA}}$ galaxies of Le Fèvre et al. (2019) show a NIV] emission line that is more luminous than NV, but both lack an OVI detection. With the exception of the young SFG of Marques-Chaves et al. (2021; which shows P Cygni profiles in both OVI and NV, but no NIV] emission line detection), all the sources with NV and OVI detections are AGN. Because it is a high-ionization emission line, the OVI line is usually associated with AGN activity, although it has also been detected in emission in a small number of extreme SFG (Otte et al. 2003; Grimes et al. 2007; Hayes et al. 2016). We report in Appendix A the complete list of the sources we use for our comparison, as well as the detected lines.

2.4. Comparison with theoretical predictions

We exploited the NIV]/NV and OVI/NV flux ratios to further investigate the origin of the additional NV emission component, as well as NIV] and OVI emission lines. Figure 3 shows the comparison of the line ratios in GS-14 (red star) with those from the AGN of Sect. 2.3 with all the three lines detected (cyan diamonds). GS-14 NIV]/NV line ratio uncertainty is shown as a black error bar and the OVI/NV lower limit is indicated with the black arrow. The contours refer to the theoretical predictions for flux ratios driven by shocks, AGN, and SF. The shock predictions (brown contours) are from the Mexican million models database (3MDB^S; Morisset et al. 2015), a compilation of shock models calculated with the code MAPPINGS and evaluated with the CLOUDY (Ferland et al. 2013) photoionization code. The SF models (green contours) are from the Gutkin et al. (2016) models and refer to a cloud illuminated by a 10 Myr old population; the nebular emission was computed with CLOUDY. Finally, the AGN predictions (blue contours) are from Feltre et al. (2016) and rely on CLOUDY to simulate the emission from a narrow-line region (NLR) cloud illuminated by the central AGN. We find that no shock model is able to reproduce the observed flux ratios of GS-14, while both SF and AGN models are compatible with the observed values. We note that because we must consider the OVI flux as a lower limit, the intrinsic OVI/NV flux ratio in GS-14 should be higher; in fact, the IGM attenuation

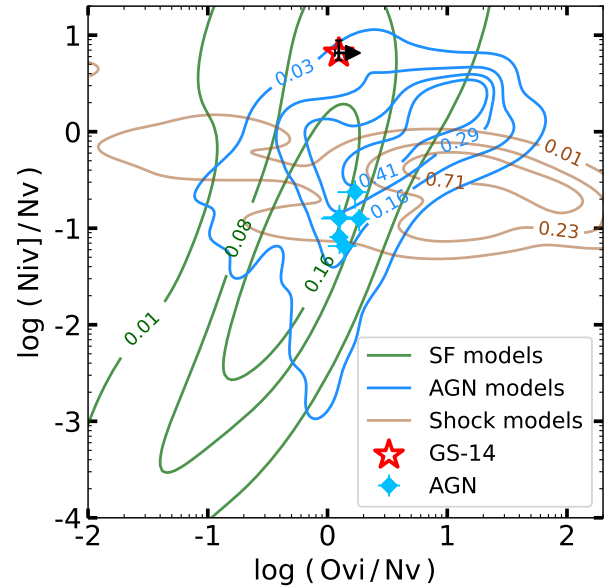


Fig. 3. Comparison of GS-14 (red star), literature AGN (cyan diamonds), and nebular theoretical predictions of the NIV]/NV and OVI/NV flux ratios. The contours represent isoproportions of the density (i.e., 8% of the probability mass lies outside of the contour drawn for 0.08). Brown contours refer to shock predictions from the Morisset et al. (2015) 3MDB^S database, green contours to SF models from Gutkin et al. (2016), and blue contours to AGN emission as computed by Feltre et al. (2016). Literature AGN are the sources described in Sect. 2.3 and in Appendix A with all the three lines detected. No shock model is able to reproduce the GS-14 line ratios; SF and AGN can both be at the origin of the observed nebular emission. As the GS-14 OVI line is not corrected for the IGM attenuation, we have only a lower limit on its flux, thus a lower limit on the OVI/NV ratio (black arrow).

at OVI wavelength for a $z \sim 5.5$ source could be as high as a factor 4 (e.g., Inoue et al. 2014) and GS-14 should move toward the region in which fewer SF models reside. Table 2 reports the parameter space explored by the shock, AGN, and SF models we used. While we cannot constrain the ionization parameter using the GS-14 flux ratios, we find that for the AGN models, only a hydrogen density of the cloud of $n_{\text{H}} \sim 10^4 \text{ cm}^{-3}$ and a metallicity $Z \leq 0.5 Z_{\odot}$ fit our data. Regarding the SF models, the observed line ratio can be reproduced only by $Z \leq 0.13 Z_{\odot}$ models. With this low metallicity, stellar models predict a much weaker P Cygni profile in the NV wind line than is observed. This suggests that the nebular emission in GS-14 is likely powered by an AGN. In the future, a definitive answer on the origin of the emission might be obtained by observing more emission lines, such as C IV 1550 Å and He II 1640 Å.

3. Photometric analysis

3.1. Photometric data

GS-14 has been observed in several photometric bands. It has been detected with the MPG-ESO Wide Field Imager (WFI; Hildebrandt et al. 2006; Erben et al. 2005), with the Infrared Spectrometer and Array Camera (ISAAC) instrument at the Very Large Telescope (VLT; Wuyts et al. 2008; Nonino et al. 2009; Retzlaff et al. 2010), with the Canada-France-Hawaii Telescope (CFHT) Wide-field InfraRed Camera (WIRC; Hsieh et al. 2012), and with the SUBARU Suprime-Cam (Cardamone et al. 2010). Regarding observations from space telescopes, GS-14

Table 2. Parameter space for the AGN, SF, and shock models.

		N_{sample}	values
AGN	$\log U_S$	5	$[-5, -1]$
	Z/Z_\odot	16	$[0.06, 4.6]$
	ξ_d	3	0.1, 0.3, 0.5
	$\log(n_{\text{H}}/\text{cm}^{-3})$	3	2, 3, 4
	α	4	$[-2, -1.2]$
SF	$\log U_S$	7	$[-1.0, -4.0]$
	Z/Z_\odot	14	$[0.006, 2.6]$
	ξ_d	1	0.3
	$\log(n_{\text{H}}/\text{cm}^{-3})$	1	2
Shock	$v_{\text{shock}}/\text{km s}^{-1}$	37	$[100, 1000]$
	$\log(n_{\text{H,pre-shock}}/\text{cm}^{-3})$	7	$[0, 4]$
	$B_{\text{transv}}/\mu\text{G}$	8	$[10^{-4}, 10]$
	Z/Z_\odot		$[0.006, 2.6]$

Notes. For each parameter, N_{sample} values are simulated in the values range. U_S refers to the ionization parameter at the Strömgen radius (see Feltre et al. 2016), Z to the metallicity, ξ_d to the dust-to-metal mass ratio, n_{H} to the cloud gas density, and α to the power-law index at UV and optical wavelengths of the AGN continuum ($S_\nu \propto \nu^\alpha$ for $0.001 \leq \lambda/\mu\text{m} \leq 0.25$). For the shock models, v_{shock} refers to the shock velocity, $n_{\text{H,pre-shock}}$ to the pre-shock density, and B_{transv} to the transverse magnetic field; the investigated metallicity parameter space is the same as in the SF models.

has detections with the Advanced Camera for Survey (ACS) and Wide Field Camera 3 (WFC3) on board the *Hubble* Space Telescope (HST; Giavalisco et al. 2004; Koekemoer et al. 2011; Grogan et al. 2011; Brammer et al. 2012; van Dokkum et al. 2013), as well as with the *Spitzer* InfraRed Array Camera (IRAC; Dickinson et al. 2003; Ashby et al. 2013; Guo et al. 2013). The complete list of photometric filters we adopted is reported in Appendix B. We refer to Faisst et al. (2020) for an in-depth description of the photometric data.

The SED of GS-14 is characterized by the evident discontinuity between the VLT/ISAAC and CFHT/WIRCAM bands and the *Spitzer*/IRAC bands, which is consistent with originating from the Balmer break (see Fig. 4). Another peculiarity is that the flux in the IRAC 1 and 2 bands is higher than the fluxes of bands 3 and 4. This is probably due to a significant contribution of the $\text{H}\beta$ + $[\text{O III}]$ and $\text{H}\alpha$ lines to the IRAC 1 and 2 fluxes.

3.2. SED fitting

To estimate the galaxy properties, we chose to use the X-CIGALE code (Yang et al. 2020, 2022), the latest version of the code investigating galaxy emission (CIGALE; Burgarella et al. 2005; Noll et al. 2009; Boquien et al. 2019) SED-fitting code, as it is quite flexible and allows us to fit the photometric data with and without the AGN component, as well as with a double stellar population. We used the Bruzual & Charlot (2003) population synthesis model with a Chabrier (2003) initial mass function, nebular emission lines, a Calzetti et al. (2000) dust attenuation law, and the Draine et al. (2014) dust models. We tested different star formation histories (SFHs): double exponential, delayed SFH, delayed SFH plus burst or quench, and constant. The AGN emission was added via the SKIRTOR models (Stalevski et al. 2012, 2016), in which the torus is modeled as a clumpy two-phases medium (we refer to Yang et al. 2020, for further details). We report in Table C.1 the complete parameter space investigated via the SED fitting.

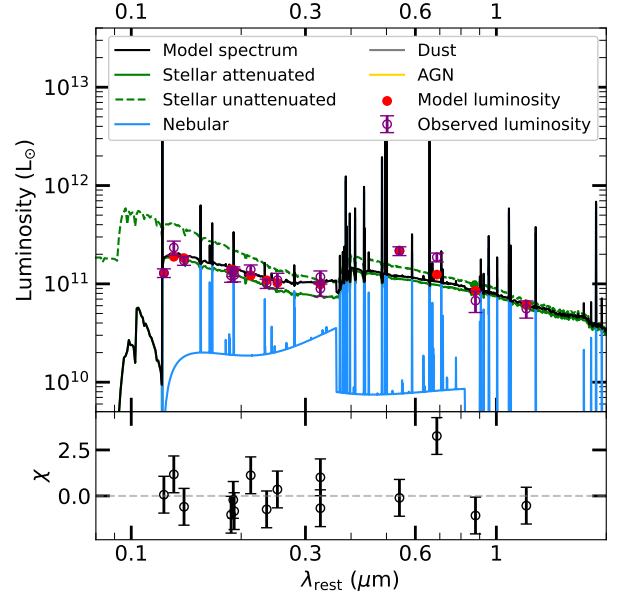


Fig. 4. X-CIGALE best-fit SED of GS-14. The fitting prefers a delayed exponential (with an optional exponential burst) SFH, with an old ($t_{\text{age}} = 680 \pm 170$ Myr) stellar population of $M_* = (4 \pm 1) \times 10^{10} M_\odot$ and a young population of 8 ± 6 Myr, which is now experiencing a burst of SF of $90 \pm 30 M_\odot \text{yr}^{-1}$. The dust and AGN component are not visible in this plot because they contribute most at $\lambda_{\text{rest}} > 3 \mu\text{m}$. The investigated parameter space is reported in Table C.1.

Table 3. GS-14 properties from photometric and spectral analyses.

	Photometric	Spectral
$\log(M_*^{\text{tot}}/M_\odot)$	$10.62^{+0.10}_{-0.13}$	
$\log(M_*^{\text{old}}/M_\odot)$	$10.61^{+0.10}_{-0.14}$	
$\log(M_*^{\text{young}}/M_\odot)$	8.7 ± 0.1	$7.7^{+0.1}_{-0.2}$
age_*^{old} (Myr)	680 ± 170	
age_*^{young} (Myr)	8 ± 6	2.7 ± 0.1
SFR (M_\odot/yr)	90 ± 30	
SFR^{MS} (M_\odot/yr)	~ 200	
$SFR^{[\text{C II}]}$ (M_\odot/yr)		16^{+14}_{-7}
SFR^{UV} (M_\odot/yr)	26 ± 5	
Z/Z_\odot	< 0.2	0.5
f_{mol}	$0.10^{+0.13}_{-0.06}$	
$E(B - V)$	0.05	0.05
$\log(L_{\text{bol,AGN}}^{\text{SED}}/\text{erg s}^{-1})$	< 44.5	
$\log(L_{\text{bol,AGN}}^{\text{X-ray}}/\text{erg s}^{-1})$	< 43.5	

Notes. M_*^{tot} , M_*^{old} , and M_*^{young} refer to the total, old, and young population, respectively. age_*^{old} and age_*^{young} refer to the age of the old and young stellar population. SFR refers to the instantaneous SFR from the SED fitting, SFR^{MS} to the expected SFR for an MS galaxy of similar mass and redshift, obtained using the Speagle et al. (2014) MS, $SFR^{[\text{C II}]}$ refers to the SFR estimated from the [C II] luminosity and using the Schaerer et al. (2020) relations of Fig. 3, and SFR^{UV} to the SFR obtained from the UV luminosity. Z refers to the metallicity. The molecular gas fraction f_{mol} was computed with the M_{molgas} of Dessauges-Zavadsky et al. (2020). The $E(B - V)$ in the Photometric column was derived from the SED fitting by Faisst et al. (2020), while the one in the Spectral column from the VIMOS spectrum as described in Sect. 2.2. $L_{\text{bol,AGN}}^{\text{SED}}$ and $L_{\text{bol,AGN}}^{\text{X-ray}}$ are the AGN bolometric luminosity derived from the SED fitting and from the *Chandra* X-ray flux upper limit, assuming the bolometric correction from Lusso et al. (2012), respectively.

Figure 4 shows the best-fit model for GS-14, with a delayed SFH, a stellar mass of $M_* = (4 \pm 1) \times 10^{10} M_\odot$, a stellar age of 680 ± 170 Myr, and a burst of SF of $\text{SFR} = 90 \pm 30 M_\odot \text{yr}^{-1}$ in the last 8 ± 6 Myr. We find that the stellar mass, age of the galaxy, and bulk of the SFH are well constrained and do not depend heavily on the presence of AGN or of a double population. Although the fitting is acceptable with a single population ($\chi^2 \sim 2.7$), we obtain a better fit when a recent burst in the SFH ($\chi^2 = 1.6$) is added. In particular, the presence of a younger population allows us to better fit the higher fluxes of the IRAC 1 and 2 bands (with respect to IRAC 3 and 4) because the H β and H α lines of the young stars contribute significantly to the IRAC 1 and 2 fluxes.

The fitting does not reveal any significant contribution from an AGN. When AGN models are used, the SED fitting constantly prefers low-luminosity type 2 AGN models, with an AGN contribution to the optical-UV six orders of magnitude lower than the stellar emission. We note, however, that we do not have any coverage in the mid-IR, where the warm dust heated by the AGN should contribute most. The SED fitting still allows us to exclude that a type 1 AGN is present, as it would contribute significantly in the optical-UV where we have an optimal photometric coverage, but leaves open the possibility of a moderate- or low-luminosity obscured AGN. This is consistent with the narrow-line profiles observed in GS-14 (Ly α and N V).

As sanity check, we also performed an SED fitting with the SED3FIT code (da Cunha et al. 2008; Berta et al. 2013), but without the option of a double population. We find that the stellar mass and SFR are compatible with those from X-CIGALE within the uncertainties. Similarly, no significant AGN contribution is detected.

4. Discussion and conclusions

We find several clues indicating that GS-14 has a double stellar population. The P Cygni profile in the N V line suggests the presence of a young population of massive stars. The fitting of the line profile provides an age of 2.7 ± 0.1 Myr and a mass of $(5 \pm 1) \times 10^7 M_\odot$. Moreover, the best SED fitting is obtained for a double population, with a 680 ± 170 Myr old population of $(4 \pm 1) \times 10^{10} M_\odot$ and a young (8 ± 6 Myr old) population of $(5.6 \pm 0.1) \times 10^8 M_\odot$ (see Table 3). In this scenario, the old population dominates and accounts for most of the stellar mass of the galaxy (similar to what was found by Laporte et al. 2021; Harikane et al. 2022; Matthee et al. 2022). It is responsible for the Balmer break and for the continuum at $\lambda_{\text{rest}} \gtrsim 3000$ Å. The young population is linked to the ongoing SF and produces the P Cygni profile and most of the continuum at ~ 2000 Å. The low cold-gas fraction of GS-14 of $f_{\text{mol}} \sim 0.10^{+0.13}_{-0.06}$, derived from the [C II] 158 μm emission (see Dessauges-Zavadsky et al. 2020) and the SED-fitting stellar mass favors the scenario that GS-14 is composed mostly of an old and evolved stellar population that formed ~ 600 Myr after the Big Bang, which has already consumed or expelled most of its original gas reservoir. We exclude the alternative origin of the N V P Cygni profile, that is, a BAL-QSO absorption feature mimicking a P Cygni profile, as there is no observational evidence that GS-14 could be a type 1 QSO and the spectra show no signs of absorption features (e.g., Ly α , C IV 1550 Å, O VI 1032 Å, or Si IV 1394, 1403 Å; Vito et al. 2022; Vietri et al. 2022).

The specific SFR (sSFR = SFR/M_*) of GS-14 is $\log(\text{sSFR}/\text{yr}^{-1}) = 8.7^{+0.1}_{-0.2}$. At this redshift, and considering the mass from SED-fitting, the SFR for an MS galaxy is $\text{SFR}^{\text{MS}} \sim$

$200 M_\odot \text{yr}^{-1}$ (Speagle et al. 2014), with the lower boundary of its 1σ dispersion at $\sim 60 M_\odot \text{yr}^{-1}$; hence GS-14 with its $\text{SFR} = 90 \pm 30 M_\odot \text{yr}^{-1}$, while below the average MS, is still within its dispersion. From the SFH derived with the SED fitting without considering the recent episode of SF, the SFR should be $\sim 1 M_\odot \text{yr}^{-1}$, thus GS-14 would be $>4\sigma$ below the MS, in the locus of quiescent galaxies. The new episode of SF has moved GS-14 up toward the MS, although it should last only a few tens of million years due to its short depletion time ($t_{\text{depl}} = M_{\text{molgas}}/\text{SFR} = 80^{+130}_{-60}$ Myr). This kind of up-and-down movement in the $\text{SFR}-M_*$ plane is expected: Tacchella et al. (2016) and Orr et al. (2019) suggested based on simulations that the MS dispersion can be originated by similar oscillations in sSFR on timescales $\sim 0.4 t_{\text{Hubble}}$.

The GS-14 N V line profile shows an emission component in addition to the P Cygni profile we fit. The comparison of the observed N V EW with N V equivalent widths from BPASS and S99 models allows us to exclude that the origin of the whole N V emission lies in stellar winds. This additional emission component therefore comes from nebular emission, but it can have various origins, depending on which process causes the radiation field that illuminates the gas. On the one hand, a shock origin can be excluded as the GS-14 flux ratios of N IV]/N V and O VI]/N V are not compatible with shock-related models (Fig. 3). On the other hand, models of AGN or SF are both able to reproduce the observed flux ratios, as shown in Fig. 3. However, we note that an AGN origin is more likely because the high-ionization potential of the O VI requires extreme conditions for it to be of stellar origin. Moreover, we found just one star-forming galaxy in the literature (Marques-Chaves et al. 2021) with both O VI and N V, all the remaining sources with these two lines are AGN. Finally, all the sources with all the three O VI, N V, and N IV] lines are AGN (Table A.1). While none of this is sufficient proof, the list of reasons strongly indicates an AGN origin for the GS-14 nebular emission. The lack of an X-ray detection for GS-14 in deep *Chandra* data and the fact that the SED fitting does not show a significant contribution from the AGN reveals that this AGN probably is of type 2. Obscured (type 2) AGN are more difficult to detect in the X-rays, but can be identified by their high ionization lines and/or by their mid-IR emission. Exploiting the X-ray flux upper limit and assuming a power-law spectrum (without AGN obscuration) for the X-ray emission with a photon index of $\Gamma = 1.8$ ($F(E) \propto E^{1-\Gamma}$), we derive a 1σ upper limit on the rest frame 2–10 keV luminosity of the AGN: $\log(L_{2-10\text{keV}}/\text{erg s}^{-1}) < 42.5$. Assuming the bolometric correction of Lusso et al. (2012), we have an upper limit on the AGN bolometric luminosity of $\log(L_{\text{bol,AGN}}^{\text{X-ray}}/\text{erg s}^{-1}) < 43.5$. The upper limit on the AGN bolometric luminosity derived from the SED fitting is $\log(L_{\text{bol,AGN}}^{\text{SED}}/\text{erg s}^{-1}) < 44.5$. AGN activity might also be a possible explanation for GS-14 extreme low content of molecular gas. A strong past phase of nuclear activity, possibly triggered by the first episode of SF, may have expelled or heated up the molecular gas, hence lowered the f_{mol} significantly and quenched the SF. The low-power AGN signature we witness now could be the last remnant of this past, more powerful, AGN activity.

Our interpretation paints an intriguing picture of GS-14: this $z \sim 5.5$ source is an already evolved galaxy that may have formed 600 Myr after the Big Bang and that now experiences a second burst of SF. It also carries signatures of obscured AGN activity.

Future observations could shed more light on the AGN contribution in GS-14, especially if those observations were

to target the mid- and far-IR part of the SED (60 μm –3 mm observer-frame), where its emission should peak, or where it might at least be disentangled from that of SF. GS-14 also deserves additional high-resolution observations with ALMA: the [C II] 158 μm is detected but not resolved, and the far-IR continuum detection (which is missing for now) would place more stringent constraints on the SF emission and the AGN contribution. Furthermore, GS-14 is the only ALPINE source with indications of obscured AGN activity, which means that follow-up with deeper and higher-resolution ALMA observations is even more important and rewarding. Finally, deep rest-UV spectroscopy, targeting medium- and high-ionization lines, such as C IV 1550 \AA , He II 1640 \AA , and C III] 1908 \AA , and exploiting their line ratio diagram, could provide the final evidence of whether the radiation field in GS-14 is dominated by the AGN activity or by a young stellar population. GS-14 was recently observed with the NIRSPEC on board the *James Webb* Space Telescope as part of the GTO program n.1216, and hopefully, the origin of its emission will be definitively unveiled.

Acknowledgements. G.C.J. acknowledges funding from ERC Advanced Grant 789056 “FirstGalaxies” under the European Union’s Horizon 2020 research and innovation programme. A.F. acknowledges the support from grant PRIN MIUR 2017-20173ML3WW_001. E.I. acknowledges funding by ANID FONDECYT Regular 1221846. M.R. acknowledges support from the Narodowe Centrum Nauki (UMO-2020/38/E/ST9/00077).

References

- Appenzeller, I., Stahl, O., Tapken, C., Mehlert, D., & Noll, S. 2005, *A&A*, **435**, 465
- Ashby, M. L. N., Willner, S. P., Fazio, G. G., et al. 2013, *ApJ*, **769**, 80
- Baldwin, J. A., Hamann, F., Korista, K. T., et al. 2003, *ApJ*, **583**, 649
- Bañados, E., Venemans, B. P., Decarli, R., et al. 2016, *ApJS*, **227**, 11
- Barchiesi, L., Pozzi, F., Vignali, C., et al. 2021, *PASA*, **38**, e033
- Bentz, M. C., Osmer, P. S., & Weinberg, D. H. 2004, *IAU Symp.*, **222**, 515
- Berta, S., Lutz, D., Santini, P., et al. 2013, *A&A*, **551**, A100
- Béthermin, M., Fudamoto, Y., Ginolfi, M., et al. 2020, *A&A*, **643**, A2
- Bischetti, M., Feruglio, C., D’Odorico, V., et al. 2022, *Nature*, **605**, 244
- Boquien, M., Burgarella, D., Roehly, Y., et al. 2019, *A&A*, **622**, A103
- Borguet, B. C. J., Edmonds, D., Arav, N., Benn, C., & Chamberlain, C. 2012, *ApJ*, **758**, 69
- Brammer, G. B., van Dokkum, P. G., Franx, M., et al. 2012, *ApJS*, **200**, 13
- Bruzual, G., & Charlot, S. 2003, *MNRAS*, **344**, 1000
- Burgarella, D., Buat, V., & Iglesias-Páramo, J. 2005, *MNRAS*, **360**, 1413
- Calzetti, D., Armus, L., Bohlin, R. C., et al. 2000, *ApJ*, **533**, 682
- Cardamone, C. N., van Dokkum, P. G., Urry, C. M., et al. 2010, *ApJS*, **189**, 270
- Cassata, P., Morselli, L., Faisst, A., et al. 2020, *A&A*, **643**, A6
- Chabrier, G. 2003, *PASP*, **115**, 763
- Cicone, C., Maiolino, R., Sturm, E., et al. 2014, *A&A*, **562**, A21
- da Cunha, E., Charlot, S., & Elbaz, D. 2008, *MNRAS*, **388**, 1595
- Dessauges-Zavadsky, M., Ginolfi, M., Pozzi, F., et al. 2020, *A&A*, **643**, A5
- Dhanda, N., Baldwin, J. A., Bentz, M. C., & Osmer, P. S. 2007, *ApJ*, **658**, 804
- Dickinson, M., & Giavalisco, M., & GOODS Team 2003, in *The Mass of Galaxies at Low and High Redshift*, eds. R. Bender, & A. Renzini (Berlin: Springer), 324
- Dietrich, M., & Wilhelm-Erkens, U. 2000, *A&A*, **354**, 17
- Dietrich, M., Appenzeller, I., Hamann, F., et al. 2003, *A&A*, **398**, 891
- Dors, O. L., Cardaci, M. V., Hägele, G. F., & Krabbe, Á. C. 2014, *MNRAS*, **443**, 1291
- Draine, B. T., Aniano, G., Krause, O., et al. 2014, *ApJ*, **780**, 172
- Erben, T., Schirmer, M., Dietrich, J. P., et al. 2005, *Astron. Nachr.*, **326**, 432
- Faisst, A. L., Schaefer, D., Lemaux, B. C., et al. 2020, *ApJS*, **247**, 61
- Fan, X., Strauss, M. A., Richards, G. T., et al. 2006, *AJ*, **131**, 1203
- Feltre, A., Charlot, S., & Gutkin, J. 2016, *MNRAS*, **456**, 3354
- Ferland, G. J., Porter, R. L., van Hoof, P. A. M., et al. 2013, *Rev. Mex. Astron. Astrophys.*, **49**, 137
- Ferrarese, L., & Merritt, D. 2000, *ApJ*, **539**, L9
- Feruglio, C., Maiolino, R., Piconcelli, E., et al. 2010, *A&A*, **518**, L155
- Fontanot, F., Cristiani, S., Monaco, P., et al. 2007, *A&A*, **461**, 39
- Fosbury, R. A. E., Humphrey, A., Villar-Martín, M., et al. 2003, in *The Mass of Galaxies at Low and High Redshift*, eds. R. Bender, & A. Renzini (Springer), 308
- Gebhardt, K., Bender, R., Bower, G., et al. 2000, *ApJ*, **539**, L13
- Giacconi, R., Zirm, A., Wang, J., et al. 2002, *ApJS*, **139**, 369
- Giallongo, E., Grazian, A., Fiore, F., et al. 2019, *ApJ*, **884**, 19
- Giavalisco, M., Ferguson, H. C., Koekemoer, A. M., et al. 2004, *ApJ*, **600**, L93
- Glikman, E., Djorgovski, S. G., Stern, D., Bogosavljević, M., & Mahabal, A. 2007, *ApJ*, **663**, L73
- Grazian, A., Giallongo, E., Fiore, F., et al. 2020, *ApJ*, **897**, 94
- Grimes, J. P., Heckman, T., Strickland, D., et al. 2007, *ApJ*, **668**, 891
- Grogin, N. A., Kocevski, D. D., Faber, S. M., et al. 2011, *ApJS*, **197**, 35
- Grupponi, C., Pozzi, F., Rodighiero, G., et al. 2013, *MNRAS*, **432**, 23
- Guo, Y., Ferguson, H. C., Giavalisco, M., et al. 2013, *ApJS*, **207**, 24
- Gutkin, J., Charlot, S., & Bruzual, G. 2016, *MNRAS*, **462**, 1757
- Hainline, K. N., Shapley, A. E., Greene, J. E., & Steidel, C. C. 2011, *ApJ*, **733**, 31
- Harikane, Y., Inoue, A. K., Mawatari, K., et al. 2022, *ApJ*, **929**, 1
- Hayes, M., Melinder, J., Östlin, G., et al. 2016, *ApJ*, **828**, 49
- Hildebrandt, H., Erben, T., Dietrich, J. P., et al. 2006, *A&A*, **452**, 1121
- Hopkins, P. F., Lidz, A., Hernquist, L., et al. 2007, *ApJ*, **662**, 110
- Hsieh, B.-C., Wang, W.-H., Hsieh, C.-C., et al. 2012, *ApJS*, **203**, 23
- Inoue, A. K., Shimizu, I., Iwata, I., & Tanaka, M. 2014, *MNRAS*, **442**, 1805
- Jaskot, A. E., Oey, M. S., Scarlata, C., & Dowd, T. 2017, *ApJ*, **851**, L9
- Koekemoer, A. M., Faber, S. M., Ferguson, H. C., et al. 2011, *ApJS*, **197**, 36
- Koptelova, E., Hwang, C.-Y., Malkan, M. A., & Yu, P.-C. 2019, *ApJ*, **882**, 144
- Kormendy, J., & Ho, L. C. 2013, *ARA&A*, **51**, 511
- Kormendy, J., & Richstone, D. 1995, *ARA&A*, **33**, 581
- Laporte, N., Meyer, R. A., Ellis, R. S., et al. 2021, *MNRAS*, **505**, 3336
- Le Fèvre, O., Lemaux, B. C., Nakajima, K., et al. 2019, *A&A*, **625**, A51
- Le Fèvre, O., Béthermin, M., Faisst, A., et al. 2020, *A&A*, **643**, A1
- Leitherer, C., Schaefer, D., Goldader, J. D., et al. 1999, *ApJS*, **123**, 3
- Lin, Y.-H., Scarlata, C., Hayes, M., et al. 2022, *MNRAS*, **509**, 489
- Lusso, E., Comastri, A., Simmons, B. D., et al. 2012, *MNRAS*, **425**, 623
- Magorrian, J., Tremaine, S., Richstone, D., et al. 1998, *AJ*, **115**, 2285
- Marques-Chaves, R., Schaefer, D., Álvarez-Márquez, J., et al. 2021, *MNRAS*, **507**, 524
- Matthee, J., Feltre, A., Maseda, M., et al. 2022, *A&A*, **660**, A10
- McGreer, I. D., Clément, B., Mainali, R., et al. 2018, *MNRAS*, **479**, 435
- McKernan, B., Yaqoob, T., & Reynolds, C. S. 2007, *MNRAS*, **379**, 1359
- McLure, R. J., Pentericci, L., Cimatti, A., et al. 2018, *MNRAS*, **479**, 25
- Morriset, C., Delgado-Inglada, G., & Flores-Fajardo, N. 2015, *Rev. Mex. Astron. Astrofis.*, **51**, 103
- Noll, S., Burgarella, D., Giovannoli, E., et al. 2009, *A&A*, **507**, 1793
- Nonino, M., Dickinson, M., Rosati, P., et al. 2009, *ApJS*, **183**, 244
- Orr, M. E., Hayward, C. C., & Hopkins, P. F. 2019, *MNRAS*, **486**, 4724
- Otte, B., Murphy, E. M., Howk, J. C., et al. 2003, *ApJ*, **591**, 821
- Patrício, V., Richard, J., Verhamme, A., et al. 2016, *MNRAS*, **456**, 4191
- Prinza, R. K., & Howarth, I. D. 1986, *ApJS*, **61**, 357
- Raiter, A., Fosbury, R. A. E., & Teimoorinia, H. 2010, *A&A*, **510**, A109
- Retzlaff, J., Rosati, P., Dickinson, M., et al. 2010, *A&A*, **511**, A50
- Rupke, D. S., Veilleux, S., & Sanders, D. B. 2005, *ApJS*, **160**, 115
- Schaefer, D., Ginolfi, M., Béthermin, M., et al. 2020, *A&A*, **643**, A3
- Schartmann, M., Meisenheimer, K., Camenzind, M., Wolf, S., & Henning, T. 2005, *A&A*, **437**, 861
- Speagle, J. S., Steinhardt, C. L., Capak, P. L., & Silverman, J. D. 2014, *ApJS*, **214**, 15
- Spergel, D. N., Verde, L., Peiris, H. V., et al. 2003, *ApJS*, **148**, 175
- Stalevski, M., Fritz, J., Baes, M., Nakos, T., & Popovic, L. C. 2012, *Publications de l’Observatoire Astronomique de Beograd*, **91**, 235
- Stalevski, M., Ricci, C., Ueda, Y., et al. 2016, *MNRAS*, **458**, 2288
- Stanway, E. R., & Eldridge, J. J. 2018, *MNRAS*, **479**, 75
- Stark, D. P., Richard, J., Siana, B., et al. 2014, *MNRAS*, **445**, 3200
- Tacchella, S., Dekel, A., Carollo, C. M., et al. 2016, *MNRAS*, **458**, 242
- Tang, M., Stark, D. P., Chevallard, J., et al. 2021, *MNRAS*, **501**, 3238
- van Dokkum, P., Brammer, G., Momcheva, I., Skelton, R. E., & Whitaker, K. E. 2013, arXiv e-prints [arXiv:1305.2140]
- Vanzella, E., Cristiani, S., Dickinson, M., et al. 2006, *A&A*, **454**, 423
- Vanzella, E., Grazian, A., Hayes, M., et al. 2010, *A&A*, **513**, A20
- Vanzella, E., Nonino, M., Cupani, G., et al. 2018, *MNRAS*, **476**, L15
- Vietri, G., Misawa, T., Piconcelli, E., et al. 2022, *A&A*, **668**, A87
- Vito, F., Mignoli, M., Gilli, R., et al. 2022, *A&A*, **663**, A159
- Weymann, R. J., Morris, S. L., Foltz, C. B., & Hewett, P. C. 1991, *ApJ*, **373**, 23
- Wiklund, T., Dickinson, M., Ferguson, H. C., et al. 2008, *ApJ*, **676**, 781
- Wuyts, S., Labbé, I., Förster Schreiber, N. M., et al. 2008, *ApJ*, **682**, 985
- Yang, G., Boquien, M., Buat, V., et al. 2020, *MNRAS*, **491**, 740
- Yang, G., Boquien, M., Brandt, W. N., et al. 2022, *ApJ*, **927**, 192
- Zana, T., Gallerani, S., Carniani, S., et al. 2022, *MNRAS*, **513**, 2118

Appendix A: O VI, N V, N IV] literature sources

Table A.1. Compilation of literature sources with O VI, N V, or N IV] emission lines.

	ID	z	O VI	N V	N IV]	Ref
	GS+14	5.55	✓	✓ <i>p</i>	✓	This work
AGN	Q0353-383	1.96	✓	✓	✓	Baldwin et al. (2003)
	DLS1053-0528	4.02		×	✓	Glikman et al. (2007)
	NDWFS1433	3.88		✓	✓	Glikman et al. (2007)
	UDS24561	3.21	✓	×	×	Tang et al. (2021)
	33 NL AGN	2 – 3	✓	✓	✓	Hainline et al. (2011)
	12 Seyfert 2	0 – 4		✓60%		Dors et al. (2014)
	59 radio-galaxies	0 – 4		✓25%		Dors et al. (2014)
	10 QSO2	0 – 4		✓70%		Dors et al. (2014)
	S82-20	3.08	✓	✓		Lin et al. (2022)
	J1254+0241	1.8		✓	✓	Dhanda et al. (2007)
	J1546-5253	2.0		✓	✓	Dhanda et al. (2007)
	J1553+0056	2.63		✓ <i>p</i>	×	Appenzeller et al. (2005)
	16 QSO	2.4 – 3.8	✓26%	✓		Dietrich & Wilhelm-Erkens (2000)
	11 QSO	3.9 – 5.0	✓73%	✓	✓73%	Dietrich et al. (2003)
	PSO J006+39	6.61		✓	×	Koptelova et al. (2019)
	J1512+119	2.11	✓	×	×	Borguet et al. (2012)
	J000239+255034	5.80		✓		Fan et al. (2006)
	124 QSO stack	5.6 – 6.7		✓		Bañados et al. (2016)
	13 AGN stack	2 – 3.8		✓	✓	Le Fèvre et al. (2019)
galaxy	Lynx Arc	3.36	×	×	✓	Fosbury et al. (2003)
	31 stack $EW_{[C II]} > 20$	2 – 3.8		✓	✓	Le Fèvre et al. (2019)
	120 stack $10 < EW_{[C II]} < 20$	2 – 3.8		✓	✓	Le Fèvre et al. (2019)
	J141445+544631	5.42	×	×	✓	McGreer et al. (2018)
	J160810+352809	0.03		✓ <i>p</i>		Jaskot et al. (2017)
	Ion3	4.0	×	✓ <i>p</i>	×	Vanzella et al. (2018)
	17 low mass galaxies stack	1.4 – 2.9		✓	✓6%	Stark et al. (2014)
	L* lensed galaxy	3.5		✓	✓	Patrício et al. (2016)
	J0121+0025	3.24	✓ <i>p</i>	✓ <i>p</i>	×	Marques-Chaves et al. (2021)

Notes. Each row refers to a single source, a collection of sources, or a stacked spectrum. In the first case, the *ID* columns refer to the source name, in the second case, to the number and type of the sources in the collection, and in the third case, to the number of sources included in the stack. O VI, N V, and N IV] report the detection (✓) or the nondetection (×) of the respective emission line. No symbol indicates that the line falls out of the spectral range. In case of a collection of sources, the percentage refers to the fraction of sources with a detection in the reported emission lines. Finally, *p* indicates that the line exhibits a P Cygni profile.

Appendix B: Photometry

We summarize here the ground- and space-based photometric data we used for the SED fitting (see §3.2). The adopted filters as well as their wavelengths and references to the measurements are reported in Table B.1. The photometry of all ALPINE sources was collected and calibrated by Faisst et al. (2020). It comes primarily from the 3D-*HST* catalog and was corrected for Galactic extinction, point spread function size, and other biases. Some additional data that are not present in the 3D-*HST* catalog come from various observation programs in the Extended Chandra Deep Field South (Giacconi et al. (2002, ECDFS,)) and were measured and calibrated by Faisst et al. (2020). GS-14 has not been detected by MPG-ESO/WFI in band *U*38, *b*, and *v*, in the *HST*/ACS *F*435W band, by the Subaru/Suprime-Cam *IA*445, *IA*505, *IA*527, *IA*550, *IA*574, *IA*598, *IA*624, and *IA*738 filters, or by *Spitzer*/*MIPS* at 24 μ m. Regarding the X-ray bands, GS-14 is undetected in the ultradeep 7 Ms X-ray image by *Chandra* with a flux limit of 10^{-17} erg cm $^{-2}$ s $^{-1}$ in the observed frame 0.5 – 2.0 keV band (Giallongo et al. 2019). We refer to Faisst et al. (2020) for further details.

Table B.1. Photometric bands.

Observatory /Instrument	Filter	Central λ [Å]	Ref.
MPG-ESO/WFI	<i>I</i>	3633.3	1
VLT/ISAAC	<i>J^v</i>	12492.2	2
	<i>H^v</i>	16519.9	2
	<i>K_s^v</i>	21638.3	2
CFHT/WIRCam	<i>J^w</i>	12544.6	3
	<i>K_s^w</i>	21590.4	3
Subaru/Suprime-Cam	<i>IA</i> 856	8566.0	4
<i>HST</i> /ACS	<i>F</i> 814W	8058.2	5
	<i>F</i> 850LP	9181.2	6
<i>HST</i> /WFC3	<i>F</i> 125W	12516.3	7
	<i>F</i> 140W	13969.4	8
	<i>F</i> 160W	15391.1	7
<i>Spitzer</i> /IRAC	ch1	35634.3	9
	ch2	45110.1	9
	ch3	57593.4	10
	ch4	79594.9	10

Notes. For details about the data, extraction, and calibration, we refer to Faisst et al. (2020).

References. (1) Hildebrandt et al. (2006), Erben et al. (2005); (2) Wuyts et al. (2008), Retzlaff et al. (2010); (3) Hsieh et al. (2012); (4) Cardamone et al. (2010); (5) Giavalisco et al. (2004); (6) Koekemoer et al. (2011); (7) Grogin et al. (2011), Koekemoer et al. (2011); (8) Brammer et al. (2012), van Dokkum et al. (2013); (9) Ashby et al. (2013), Guo et al. (2013); (10) Dickinson et al. (2003).

Appendix C: X-CIGALE SED-fitting parameter space

Table C.1. Parameter space for the X-CIGALE SED fitting.

	N_{sample}	values	description
SFH		sfh2exp; sfhdelayed; sfhdelayedbq; sfhperiodic	double exponential; delayed SFH with optional exponential burst; delayed SFH with optional constant burst/quench; periodic SFH.
τ_{main}	3	50, 500, 1000	e-folding time of the main stellar population model in Myr.
age_{main}	6	100, 250, 500, 600, 700, 1000	Age of the main stellar population in the galaxy in Myr.
τ_{burst}	3	50, 100, 500	e-folding time of the late starburst population model in Myr.
$\text{age}_{\text{burst}}$	4	5, 10, 20, 50	Age of the late burst in Myr.
f_{burst}	4	0, 0.001, 0.01, 0.1	Mass fraction of the late burst population.
IMF		Chabrier	Initial Mass Function
Z/Z_{\odot}	4	0.03, 0.3, 1.3, 3.2	Metallicity
$\log U_{\text{S}}$	2	-2, -1	Nebular component: ionization parameter
Z_{gas}	2	0.0004, 0.004	Nebular component: gas metallicity
dust attenuation		Charlot&Fall 2000	
$A_{\text{V,ISM}}$	3	0.3, 1.7, 3.3	V-band attenuation in the interstellar medium.
μ	3	0.3, 0.5, 1.0	$A_{\text{V,ISM}} / (A_{\text{V,BC}} + A_{\text{V,ISM}})$
Dust emission		Draine+2014	
q_{PAH}	3	0.47, 2.5, 3.9	Mass fraction of PAH.
U_{min}	4	5, 10, 25, 40	Minimum radiation field.
α	1	2.0	Power-law slope $dU/dM \propto U^{\alpha}$.
γ	2	0.02, 0.1	Fraction illuminated from U_{min} to U_{max} .
AGN		Skirtor16	
$\tau_{9.7\mu\text{m}}$	5	3, 5, 7, 9, 11	Average edge-on optical depth at $9.7 \mu\text{m}$.
p	1	1.0	Power-law index of radial gradient of dust density.
q	1	1.0	Power-law index of angular gradient of dust density.
oa	1	40°	Torus half-opening angle.
R_{ratio}	1	20	Ratio of the maximum to minimum radii of the dust torus.
M_{cl}	1	0.97	Mass fraction of dust inside clumps.
i	6	$0^{\circ}, 20^{\circ}, 40^{\circ}, 60^{\circ}, 70^{\circ}, 90^{\circ}$	Viewing angle (w.r.t. the AGN axis).
disk type	1	Schartmann et al. (2005)	Disk spectrum.
δ	1	-0.36	Power-law index modifying the optical slope of the disk.
f_{AGN}	4	0.001, 0.01, 0.05, 0.1	8 – 1000 μm AGN fraction.
law	1	SMC	Extinction law of polar dust.
E(B-V)	1	0.03	E(B-V) for the extinction in the polar direction in magnitudes.
$T_{\text{dust}}^{\text{polar}}$	1	100 K	Temperature of the polar dust.
ϵ	1	1.6	Emissivity index of the polar dust.

Notes. For each parameter, N_{sample} values are simulated in the *values* range. As the best fits were obtained with a double exponential SFH (*sfh2exp*), we report only the parameter space for this SFH, while the other investigated SFHs are indicated in *SFH*: the delayed SFH (*sfhdelayed*), the delayed SFH with a burst (*sfhdelayedbq*), and the periodic SFH (*sfhperiodic*).